

Group-velocity tomography of South America and the surrounding oceans

Oleg Vdovin,¹ José A. Rial,² Anatoli L. Levshin¹ and Michael H. Ritzwoller¹

¹ *Department of Physics and CIRES, Campus Box 390, University of Colorado, Boulder, CO 80309-0390, USA.*

E-mail: ritzwoller@lemond.colorado.edu

² *Department of Geology, 319 Mitchell Hall, University of North Carolina, Chapel Hill, NC 27599-3315, USA*

Accepted 1998 August 28. Received 1998 July 12; in original form 1997 December 23

SUMMARY

This paper presents the results of a study of the dispersion characteristics of broad-band fundamental-mode surface waves propagating across South America and the surrounding oceans. Broad-band waveform data from about 765 events from 1977 to 1996 recorded at 48 individual stations have produced 7000 Rayleigh-wave and 4800 Love-wave dispersion curves. We present group-velocity maps from 20 to 150 s period for Rayleigh waves and from 20 to 100 s for Love waves. Measurement uncertainties estimated from cluster analyses average about $0.025\text{--}0.030\text{ km s}^{-1}$, but are larger for the short-period Love waves. We estimate surface resolving kernels and show that the average resolution across South America is about $6^{\circ}\text{--}8^{\circ}$ for Rayleigh waves and $7^{\circ}\text{--}10^{\circ}$ for Love waves below 100 s period but degrades at longer periods and near the periphery of the maps. The estimated maps produce a variance reduction relative to the Preliminary Reference Earth Model (PREM) of more than 90 per cent at short periods, more than 80 per cent for Rayleigh and Love waves below about 100 s period, but nearer to about 70 per cent at longer periods. Synthetic experiments are presented to estimate the bias caused by azimuthal anisotropy using the recent global model of Trampert & Woodhouse (1996). This bias, which is worse for Love than for Rayleigh waves, may be substantial (up to 5 per cent in some places), but it is expected to be largely off the continent and is not correlated with the main features of the observed maps. Many known geological and tectonic structures are observed in the group-velocity maps. Of particular note are the signatures of sedimentary basins (e.g. Maturin-Llanos Basin, Marañon-Ucayali-Madre de Dios complex, Chaco-Tarija Basin, S. Paraná Basin, the basins in the W. Caribbean and W. Gulf of Mexico), variations in crustal thickness (e.g. Andes, Altiplano, Brazilian Highlands), continental roots (e.g. Guyana and Guaporé shields, Sao Francisco Craton), and the Galapagos thermal anomaly. Comparison of the estimated group-velocity maps with those predicted by CRUST5.1/S16B30 is qualitatively good, but there are significant differences in detail that provide new information that should help to calibrate future crustal and upper-mantle models of South America.

Key words: crust, seismic tomography, South America, surface waves, upper mantle, wave propagation.

1 INTRODUCTION

Within this decade there have been vigorous efforts to produce new information about the structure of the South American crust and lithosphere. These efforts have concentrated largely on the use of data from several temporary regional seismic networks; namely, the Broad-band ANdean JOint (BANJO) experiment in the central Andean Cordillera of Bolivia and northern Chile (1994–1995), the Seismic Exploration of the

Deep Altiplano (SEDA) experiment (1994–1995), and the Brazilian Lithosphere Seismic Project (BLSP) in south-central Brazil (1992–1995). Data from these networks have provided new information about the crust (e.g. Zandt *et al.* 1995; Beck *et al.* 1996), lithosphere (e.g. James *et al.* 1993; James & Snoke 1994; Myers *et al.* 1995; Snoke & James 1997; Van der Lee *et al.* 1997), and sublithospheric upper mantle (e.g. James 1994; Clark *et al.* 1995; VanDecar *et al.* 1995; James & Assumpção 1996) between 15°S and 20°S latitude, a region that

encompasses some of the most striking physiographic features on the South American continent, including the central Andean Cordillera of Bolivia and Northern Chile, the Altiplano, the Chaco and Paraná Basins, and the Sao Francisco Craton. In addition, teleseismic studies (e.g. Dorbath *et al.* 1993; Comte *et al.* 1994; Engdahl *et al.* 1995, 1997) and refraction surveys (e.g. Wigger *et al.* 1994) along the central Andes have provided complementary information about the crust and subducting lithosphere.

Even with these efforts, the seismic structure of the crust and upper mantle underlying South America remains rather poorly characterized as a whole, particularly in comparison with North America and Eurasia. This is partially ameliorated by the improved quality and resolution of global-scale studies such as recent phase-velocity maps (e.g. Trampert & Woodhouse 1995; Ekström *et al.* 1997) and new models of the crust (e.g. Nataf & Ricard 1996; Mooney *et al.* 1998) and upper mantle (e.g. Zhang & Tanimoto 1993; Grand 1994; Su *et al.* 1994; Trampert & Woodhouse 1996; Laske & Masters 1996; Li & Romanowicz 1996; Masters *et al.* 1996). Nevertheless, the deficit of information at subglobal resolutions outside the band between 15°S and 20°S means that continental-scale surface-wave studies, which have been very successfully applied to North America (e.g. Alsina *et al.* 1996; Van der Lee & Nolet 1997a,b) and Eurasia (e.g. Snieder 1988; Curtis *et al.* 1998; Griot *et al.* 1998; Ritzwoller *et al.* 1998; Ritzwoller & Levshin 1998), should produce valuable information about the crust and lithosphere under much of South America. Surface-wave studies dedicated to South America date back to James (1971), who analysed phase-velocity curves for a few paths in and adjacent to the Andes. More recently, de Souza (1995) used estimates of a number of surface-wave dispersion curves to estimate crustal shear velocities in the continental shelf off southeastern Brazil, and Snoke & James (1997) used BLSP data to constrain the crustal velocity structure beneath the Chaco and Paraná Basins.

The purpose of this study is to present the dispersion characteristics of broad-band Rayleigh (20–150 s) and Love (20–100 s) waves propagating across all of South America and the surrounding oceans. These results are presented as group-velocity maps that represent the local group velocity of a Rayleigh or Love wave at each period. The main motivation for the study is that these group-velocity maps provide new constraints on the shear-velocity structure of the crust and uppermost mantle beneath South America as well as the location of internal boundaries such as the Moho. These maps display better resolution and should be more reliable (lower variance and bias) than globally estimated dispersion maps or such maps computed from current global models of the crust and mantle. They should also help to calibrate future generations of global and regional dispersion maps and seismic models, to provide transportable data to be used in future inversions for the shear-velocity structure of South America, and to help provide a larger-scale context for smaller-scale studies.

The methods of dispersion measurement and tomography that we employ here were applied initially to Eurasia and are discussed in detail by Ritzwoller & Levshin (1998) (herein-after referred to as RL98) and Ritzwoller *et al.* (1998) (herein-after referred to as RLRE98). Two innovations are introduced here: we have developed a new method of resolution and bias analysis and we have corrected for group source time shifts

(Levshin *et al.*, in preparation). South America is a more challenging target for surface-wave dispersion studies than Eurasia. The quantity of continental seismicity is significantly lower and South America remains more poorly instrumented than Eurasia. Therefore, at least until the station distribution across the South American continent is improved substantially, surface-wave studies across the entirety of South America must be based, in part, on the use of earthquakes and stations outside the continent. Fig. 1(a) displays the locations of the 765 earthquakes and the 48 stations (GSN, GEOSCOPE networks) used in this study. Most of the earthquakes occurred after 1987 and

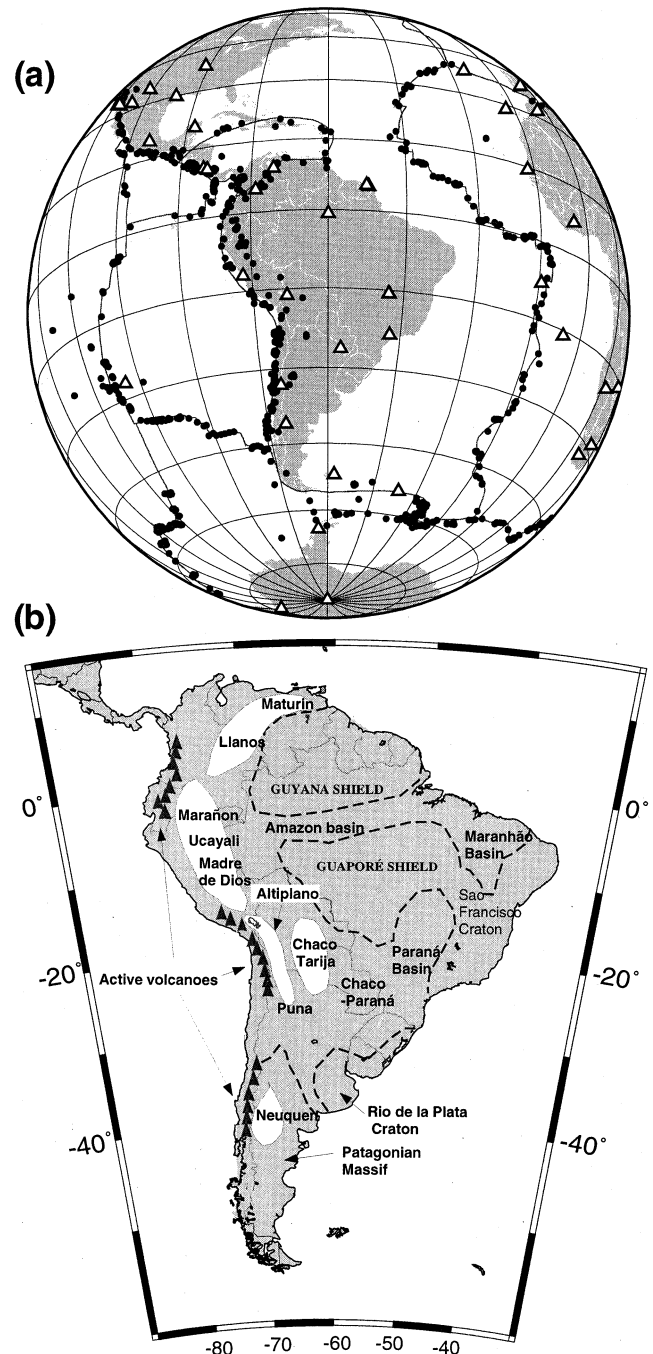


Figure 1. (a) Locations of the 765 earthquakes (filled circles) and the 48 stations (open triangles) used in this study. (b) Schematic map of South America displaying key tectonic and geological features.

have $M_s \geq 5.5$, but we also processed some smaller earthquakes on the continent and high southern latitude events from 1977 to 1987. Nevertheless, only about 213 earthquakes and 15 stations are located on or very near to the South American continent (13°N – 56°S , 82°W – 34°W).

Many notable features of the South American crust and lithosphere are observed in the group-velocity maps presented here. These include sedimentary basins at short periods (< 30 s), crustal velocity and thickness variations at intermediate periods (~ 50 s), and continental roots beneath cratons and shields at the long-period end of the study (≥ 100 s). Since the deepest-penetrating waves of this study (Rayleigh, 150 s) do not sample below about 200 km depth, this study cannot resolve deep-seated sublithospheric structures such as the hypothesized fossil plume beneath southeastern Brazil (VanDecar *et al.* 1995) or subducting slabs (e.g. Engdahl *et al.* 1995, 1997).

The outline of the paper is as follows. Section 2 presents a brief discussion of the methods of measurement and tomography. The reader is referred to RL98 for a more complete treatment. We discuss resolution and bias in Section 3. In particular, we present a new method of estimating resolution and bias and investigate the bias caused by azimuthal anisotropy on our isotropic group-velocity maps. Preliminary discussion of the group-velocity maps is the subject of Section 4.

2 DATA, MEASUREMENT AND SURFACE-WAVE TOMOGRAPHY

We obtained group-traveltime, phase-traveltime and spectral-amplitude measurements by use of an interactive frequency–time analysis (FTAN) method (e.g. Dziewonski *et al.* 1969; Landisman *et al.* 1969; Levshin *et al.* 1972; Cara 1973; Feng & Teng 1983; Russell *et al.* 1988; Levshin *et al.* 1992; RL98). Group velocity and phase velocity are computed from the group and phase traveltimes and the distance between the receiver and the centroid moment tensor (CMT) location (Dziewonski *et al.* 1981). (Only the group traveltimes are used here.) Distances are measured on the reference ellipsoid and all times are referenced to the CMT time. [Synthetic experiments indicate that only small differences in the group-velocity maps result from the use of preliminary determination of epicentres (PDE) or International Seismological Centre (ISC) times.] RL98 describes the measurement procedure in detail. We measured about 7000 Rayleigh-wave and 4800 Love-wave dispersion curves using FTAN. Fig. 2(a) displays the number of measurements for Rayleigh and Love waves as a function of period and Fig. 2(b) shows the average path length of the measurements as a function of period and wave type. An analyst oversees every measurement. Biases at long periods that result from sloped amplitude spectra are corrected using the method described by Levshin *et al.* (1989, 1992).

The resulting data set exhibits considerable redundancy, which allows for consistency tests, outlier rejection and the estimation of measurement uncertainties. We ‘cluster’ and compare measurements from similar paths following the procedure described by RL98. About one-third of all measurements fall within some cluster. We produce a single measurement for each cluster at each period and wave type. Clear outliers are identified as part of the cluster analysis because they disagree with other measurements from

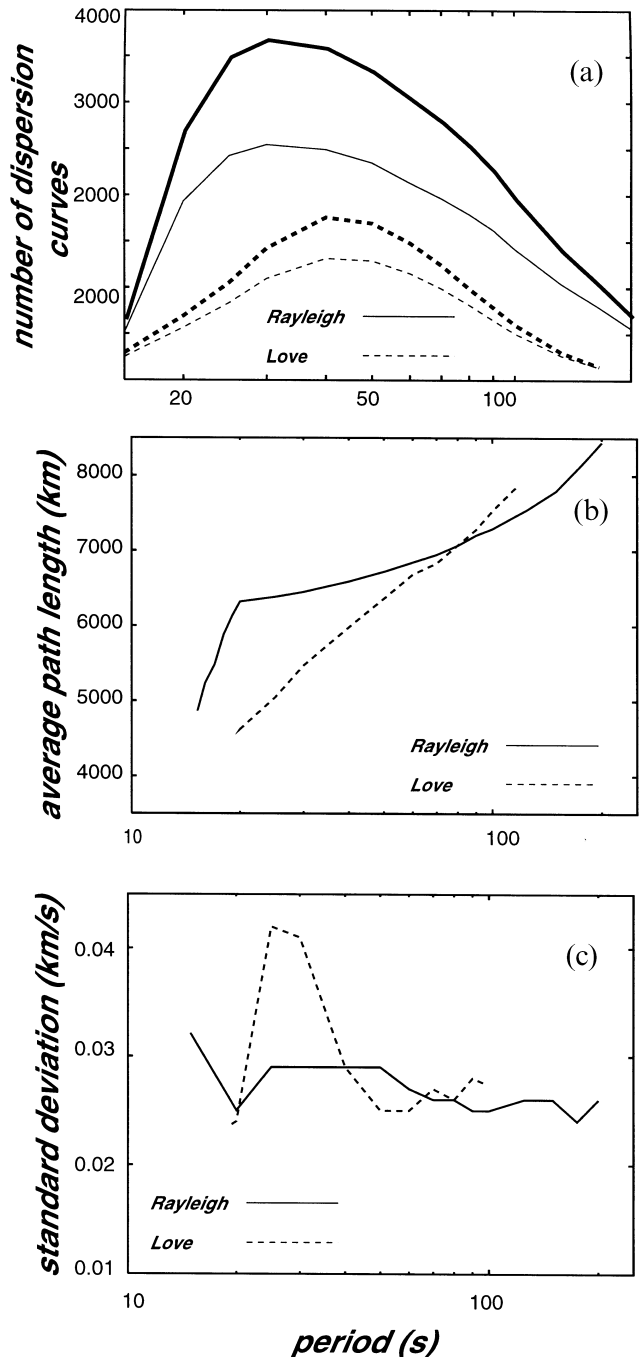


Figure 2. (a) The number of dispersion curves estimated for Rayleigh (solid) and Love (dashed) waves before (bold line) and after (thin lines) the cluster analysis. (b) Average path length after the cluster analysis (Rayleigh: solid; Love: dashed). (c) Average measurement uncertainties defined as the standard deviation of the measurements that comprise each cluster averaged over all clusters.

similar paths. Fig. 2(c) displays the standard deviation of the measurements within each cluster averaged over all clusters. We interpret this statistic as the average measurement uncertainty. Uncertainties are largely independent of period and average between about 0.025 and 0.030 km s^{-1} , except for Love waves below about 30 s where uncertainties rise to about 0.040 km s^{-1} . The rise in uncertainties for short-period Love waves is probably caused by the fact that the 20 s Love-wave

sensitivity kernel is compressed nearer to the surface than the Rayleigh wave at this period. Thus, scattering due to relatively small-scale near-surface features makes Love-wave measurements more difficult to obtain reliably. However, the decreased uncertainty for the 20 s Love wave results from the fact that most 20 s Love-wave measurements come from paths entirely confined to the continent. This simplifies the paths considerably and tends to reduce scattering. We follow RL98 in assigning data weights from the cluster uncertainties.

We use the algorithm of Ditmar & Yanovskaya (1987) and Yanovskaya & Ditmar (1990) to construct the group-velocity maps (see also Levshin *et al.* 1989, Chapter 6). This method estimates a group-velocity map $U(\theta, \phi)$ at each period and wave type by attempting to minimize the following penalty function:

$$\sum_{i=1}^N [w_i(t_i^{\text{obs}} - t_i^{\text{pred}})]^2 + \lambda \int_S |\nabla U(\theta, \phi)|^2 dA, \quad (1)$$

where

$$t_i^{\text{pred}} = \int_{p_i} U^{-1}(\theta, \phi) ds + \delta t_i^{\text{source}}. \quad (2)$$

Here, p_i represents the i th wave path, w_i is the weight associated with the i th path, which is a function of the measurement uncertainty, the number of paths within the cluster that generated the measurement, and a qualitative grade supplied by the analyst during measurement, t_i^{obs} and t_i^{pred} are the observed and predicted group traveltimes along the i th path and S is the region on which the inversion is performed. Choosing different values of the trade-off parameter, λ , changes the trade-off between the fit to the data and the ‘smoothness’ of the resulting group-velocity map. ‘Smooth’ here is defined in terms of the spatial gradient of the model. The trade-off parameter is chosen by analysing misfit and the visual characteristics of the resulting maps. Typically, we choose λ to produce a slightly underdamped map and, because the penalty function in eq. (1) does not include a second-spatial gradient term, we smooth each map *a posteriori* with a 2-D Gaussian spatial-smoothing filter. Both the resolution analysis and inversion occur separately for each period and wave type. In eq. (2), we assume that each wave path, p_i , is along the great circle linking the source and receiver and $\delta t_i^{\text{source}}$ is the group time perturbation introduced by a source group time shift (e.g. Knopoff & Schwab 1968; Levshin *et al.*, in preparation), which is computed from the CMT.

3 RESOLUTION AND BIAS

3.1 Errors related to path coverage and damping

Irrespective of theoretical errors, the resolution of the data set is dominantly a function of the path distribution (density of paths, azimuthal coverage, average path length locally) and the weighting and damping applied during inversion. Path distribution depends strongly on geographical location, period and wave type and derives principally from the nature of the data set used. Compared with Eurasia, South American path densities are lower, path lengths are longer and azimuthal coverage is less uniform. Thus, we expect lower resolutions across South America than those presented in RL98 and LLRE98 for Eurasia. In particular, the longer paths make the

shorter-period measurements (< 30 s) more difficult to obtain, and the South American maps below 30 s period are probably less reliable than the maps at the same periods across Eurasia.

Fig. 3 presents examples of the path coverage, where we plot the path density, defined as the number of paths after clustering the data that intersect each square 2° cell ($\sim 50\,000$ km²). Path densities are significantly higher for Rayleigh than for Love waves. Coverage is sufficient to construct Rayleigh-wave maps up to 150 s period but only to about 100 s for Love waves. Due to our use of data from North and Central American stations, path densities are also higher in the northern (e.g. Caribbean, Central America, Cocos Plate) and western (e.g. Eastern Nazca Plate) parts of the studied area and are lowest in the east and southeast. In particular, Love-wave path coverage in the southwestern Atlantic Ocean is very poor.

Path density is only simply related to resolution if azimuthal coverage is relatively homogeneous. Unfortunately, azimuthal distribution is notoriously inhomogeneous across much of South America and, for this reason, it would be useful to estimate resolution and bias. Checkerboard tests are commonly used to estimate resolution (e.g. RL98), but L  v  que *et al.* (1993) and others have argued that the results of these tests can be misleading and our own experience indicates that they are simply difficult to interpret unambiguously. Moreover, they do not provide information about the source or nature of the irresolution, e.g. if a cell is unresolved due to poor local coverage or due to ‘leakage’ from another nearby cell.

It is more useful to estimate spatial averaging kernels $K(\theta, \phi; \mathbf{r}_0)$ (e.g. Backus & Gilbert 1968) for each point $[\mathbf{r}_0 = (\theta_0, \phi_0)]$ on the map

$$\frac{\delta \hat{U}(\mathbf{r}_0)}{U} = \int K(\theta, \phi; \mathbf{r}_0) \frac{\delta U(\theta, \phi)}{U} d\Omega, \quad (3)$$

where $\delta \hat{U}(\mathbf{r}_0)/U$ is the estimated group-velocity variation at \mathbf{r}_0 and $\delta U(\theta, \phi)/U$ is the ‘true’ group-velocity variation across the entire map. The averaging kernel may be estimated from the resolution matrix but we prefer to infer it *a posteriori* by determining our ability to retrieve a test function centred at \mathbf{r}_0 . The test function we choose is a spatially limited 2-D Gaussian of fixed input amplitude, A , and known width, 2σ , whose centroid is moved to various positions, \mathbf{r}_0 , around the region of study. We set A equal to a 10 per cent velocity perturbation and σ is the standard deviation of the Gaussian, which we choose in the way described below. Let us call the input test function at position \mathbf{r}_0 , $G^{\text{in}}(\theta, \phi; (A, \sigma, \mathbf{r}_0)) = \delta U(\theta, \phi)/U$. We compute synthetic traveltimes through this function and invert for the estimated velocity map, $M(\theta, \phi; G^{\text{in}}) = \delta \hat{U}(\theta, \phi)/U$, with the same ray paths, weighting and damping as used at each period and wave type with the real data. If the input Gaussian is sufficiently delta-like, the estimated map is a good approximation to the averaging kernel, $M(\theta, \phi; G^{\text{in}}) \sim K(\theta, \phi; \mathbf{r}_0)$. In practice, it suffices if the width of G^{in} is somewhat less than the resolution at \mathbf{r}_0 .

The averaging kernel at \mathbf{r}_0 can be characterized in a number of ways. We fit a 2-D Gaussian, $G^{\text{fit}}(\theta, \phi; (\hat{A}, \hat{\sigma}, \hat{\mathbf{f}}))$, of variable amplitude, \hat{A} , width, $2\hat{\sigma}$, and centroid, $\hat{\mathbf{f}}$, to K and then identify the width of the best-fit Gaussian with ‘resolution’ and the difference between the centroids of the input and fitted Gaussians with the ‘bias’, $\hat{\mathbf{f}} - \mathbf{r}_0$. Fig. 4 displays the results of attempts to estimate resolution and bias using this method at three diverse geographical points for the wave paths, data

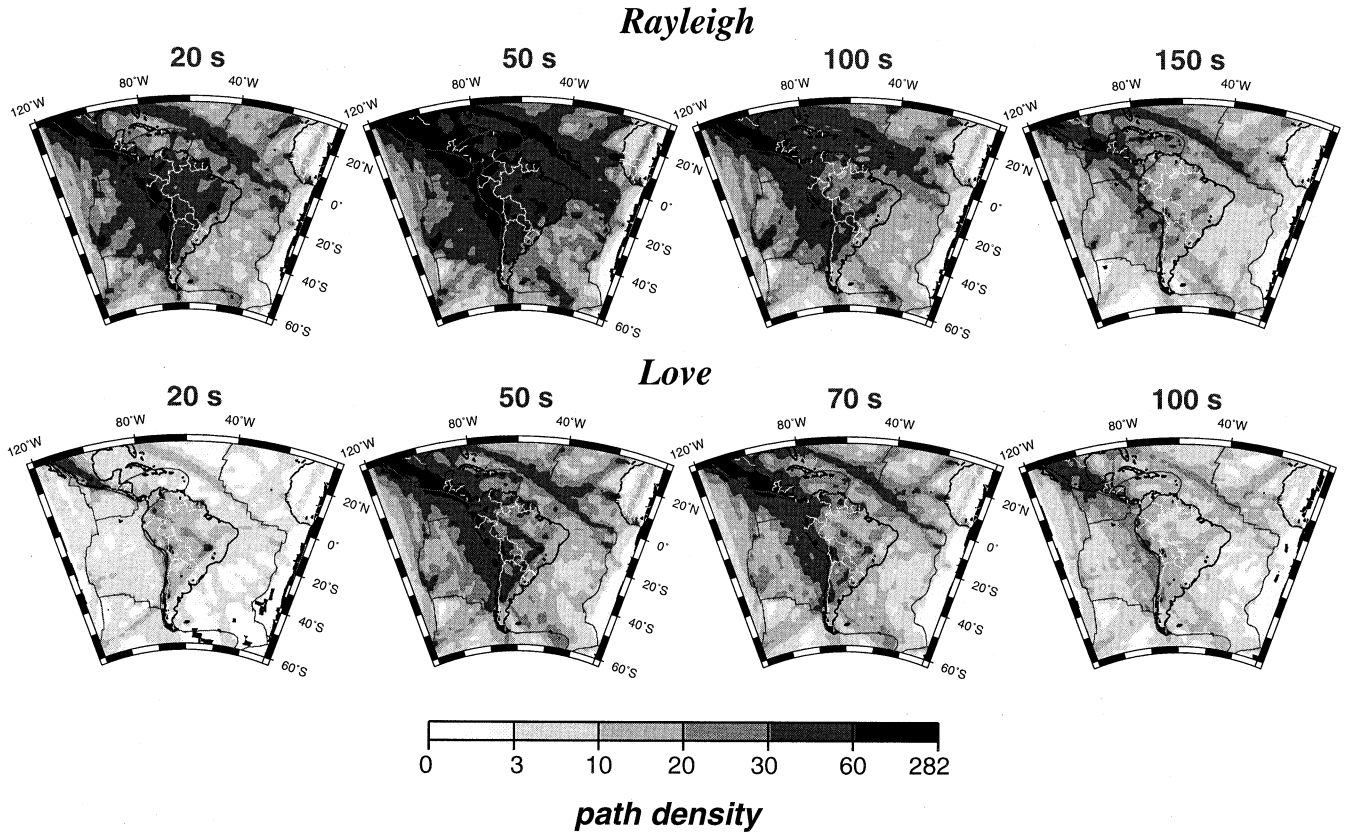


Figure 3. Path densities for Rayleigh and Love waves at the indicated periods. Path density is defined as the number of rays intersecting a 2° square cell ($\sim 50\,000\text{ km}^2$).

weights and damping applied in the 150 s Rayleigh-wave inversion. The small circles indicate the widths (2σ) of the input 2-D Gaussian test functions (G^{in}) and the grey-shaded patterns are the estimated averaging kernels. The larger circles represent the widths ($2\hat{\sigma}$) of the Gaussians fit to the averaging kernels. The width of the input Gaussian is chosen so that the estimated averaging kernel is fitted relatively well by the fitted Gaussian. We use the criterion that the root-mean-square (rms) of the difference between the estimated surface and the fitted Gaussian is about 40 per cent of the rms of the estimated surface itself. That is, $\text{rms}[K - G^{\text{fit}}]/\text{rms}[K] \sim 40$ per cent.

The relation between the resolving kernels and the input Gaussians is highly variable. In Fig. 4(a), where the test function is located on the continent near to the Colombian–Brazilian border, the resolving kernel is quite similar to the input Gaussian, although its amplitude is approximately halved. The width of the fitted Gaussian is increased to about 8° from 5° for the input Gaussian and the fitted Gaussian is shifted to the east-northeast by about 2° . The fidelity of the resolving kernel in Figs 4(b) and (c) is worse, where the input Gaussians are located off the coast, near the Galapagos Islands and in the southwest Atlantic Ocean, respectively. This is reflected in poorer resolutions and larger bias. Resolution in the southwest Atlantic is about 12° with a bias of about 8° to the north-northeast and at the Galapagos is estimated to be 9° , although bias is less than 1° .

We compile results such as those in Fig. 4 to form the maps of resolution and bias shown in Fig. 5. Not surprisingly, resolution is best where the majority of stations are located: on

the continent, in the Caribbean and in Central America. Resolution optimizes at about 40 s period for both Rayleigh and Love waves, although at any period resolution is typically better for Rayleigh than for Love waves. Fig. 6(a) displays the average resolution across the continent as a function of period and wave type. We estimate average resolution on the continent below 100 s period at 6° – 8° for Rayleigh waves and 8° – 10° for Love waves. Resolution degrades quickly for Love waves above 50 s and for Rayleigh waves above about 100 s period. Bias can be a significant fraction of the estimated resolution at each point but is typically less than about half of the resolution. The regions of greatest bias, therefore, are those that display the worst resolution. Bias in the interior of South America is usually quite low, except in the far south, at long periods in particular.

3.2 Theoretical bias: azimuthal anisotropy

There are problems other than path distribution, weighting and damping that affect the accuracy of the estimated maps; these mainly derive from errors in approximations and assumptions. We call these problems ‘theoretical errors’. There are three principal theoretical errors: (1) earthquake mislocations, (2) distortions in the 3-D wavefield due to lateral inhomogeneities, and (3) anisotropy. We have shown elsewhere (RL98) away from source regions or in source regions with significant crossing paths that emanate from other source regions. Most of South America falls into one or other of these

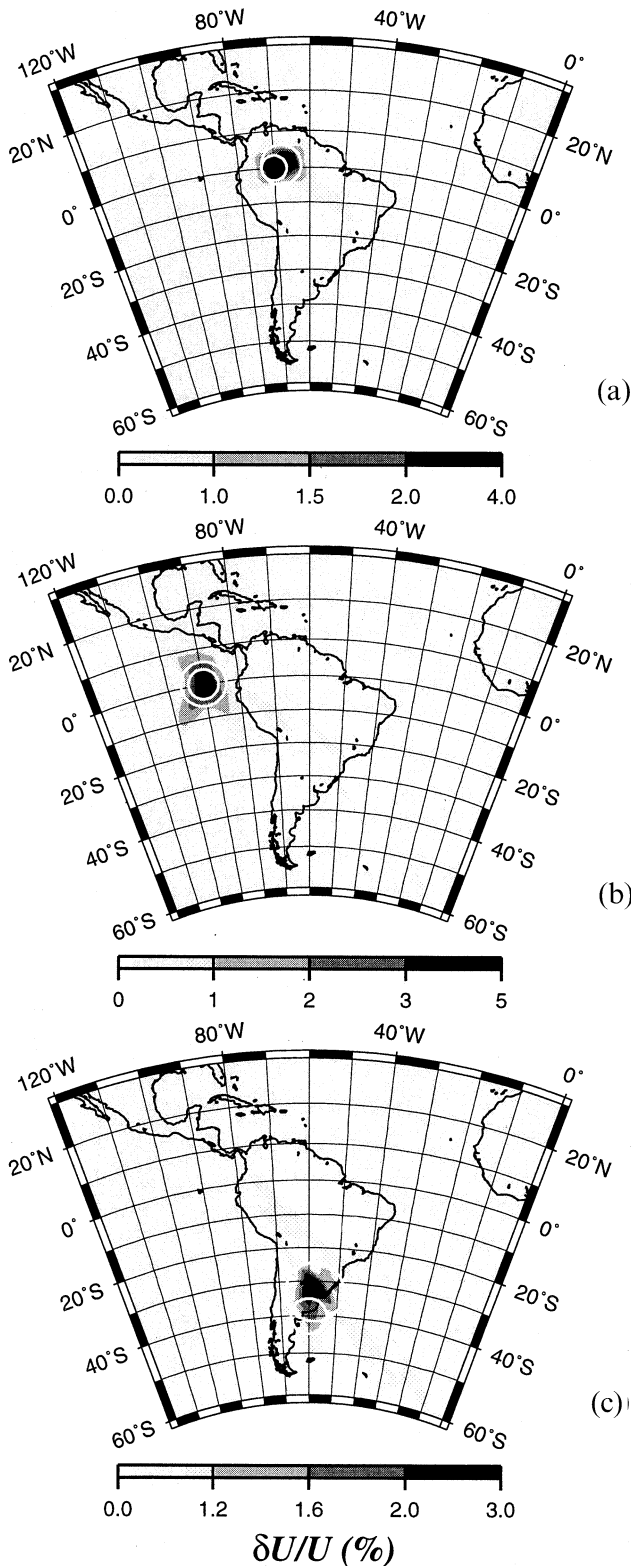


Figure 4. Three examples of the ability to estimate an input 2-D Gaussian test function using the paths, data weighting and damping for the 150 s Rayleigh wave. The location of the input Gaussian (G^{in}) is the smaller white circle plotted at the 1σ point on each plot. The peak amplitude, U , of the input Gaussian is 10 per cent. The estimated averaging kernel (K) is grey shaded with values $\delta U/U$ in per cent. The fitted Gaussian (G^{fit}) is the larger white circle plotted at the estimated 1δ point, where δ is the standard deviation of the fitted Gaussian.

two categories and, therefore, source mislocations provide a significant error in the estimated group-velocity maps except near the East Pacific Rise and the Mid-Atlantic Ridge. The second error results from phenomena that include off-great-circle propagation, multipathing, spatially extended Fresnel zones and Wielandt's distinction between dynamic and structural wavenumber and velocity (e.g. Wielandt 1993; Friederich & Wielandt 1995). These phenomena act to distort the group-velocity maps, particularly at short periods. Comparison of the outlines of known structural features to associated features on the estimated maps leads us to conclude that this distortion is typically within the stated resolution of the maps. This leaves anisotropy as a potential source of appreciable error. Because the azimuthal coverage is non-uniform across most of the region of study and because most paths possess a significant path fraction in the oceans, this study should be more sensitive to biases caused by azimuthal anisotropy than our previous studies of Eurasia.

We have performed synthetic experiments designed to estimate the nature and magnitude of the bias to isotropic group-velocity maps caused by azimuthal anisotropy. A study of the expected bias caused by azimuthal anisotropy on global phase-velocity maps has been performed by Larson *et al.* (1997). To the best of our knowledge, there are no group-velocity maps for azimuthal anisotropy across the studied region to be used in these experiments. There are, however, global phase-velocity maps of azimuthal anisotropy (e.g. Montagner & Tanimoto 1991; Trampert & Woodhouse 1996). Because the radial sensitivity kernels of phase velocities are different from those of group velocities, the use of phase-velocity azimuthal anisotropy maps as a proxy for the group-velocity maps is not optimal, but we do not expect that the general patterns of anisotropy should be greatly different. The global phase-velocity maps should, therefore, provide information about the distribution and nature of azimuthal anisotropy in group velocity within the substantial uncertainties in the phase-velocity maps. However, because the geographical patterns of anisotropy and the local orientations of fast and slow axes are much better determined than the amplitudes (Trampert, personal communication, 1997), we should pay more attention to the distribution than to the amplitude of bias.

Trampert & Woodhouse (1996) present a preliminary version of a model of the 2ψ and 4ψ components of azimuthal anisotropy produced for Rayleigh- and Love-wave phase velocities. The patterns of anisotropy for Rayleigh and Love waves in their model are similar, but the amplitudes are uniformly larger for Love waves. Because phase-velocity kernels sample deeper at each period than group-velocity kernels, the 40 and 80 s maps of Trampert & Woodhouse perhaps correspond better to group velocities between 50 and 70 s and 100 and 125 s, respectively. To estimate the bias caused by these maps of azimuthal anisotropy, we use the paths, weighting and damping from the real inversions and apply them to synthetic traveltimes computed through the anisotropic maps. We use the paths, damping, etc., for the 50 and 100 s Rayleigh and Love waves applied to the respective 40 and 80 s maps of Trampert & Woodhouse. The resulting tomographic maps represent the isotropic perturbations that would result from the traveltime anomalies imparted by the anisotropic structures. We use both the 2ψ and the 4ψ components of Trampert & Woodhouse's model, but it is the 2ψ component that produces most of the bias.

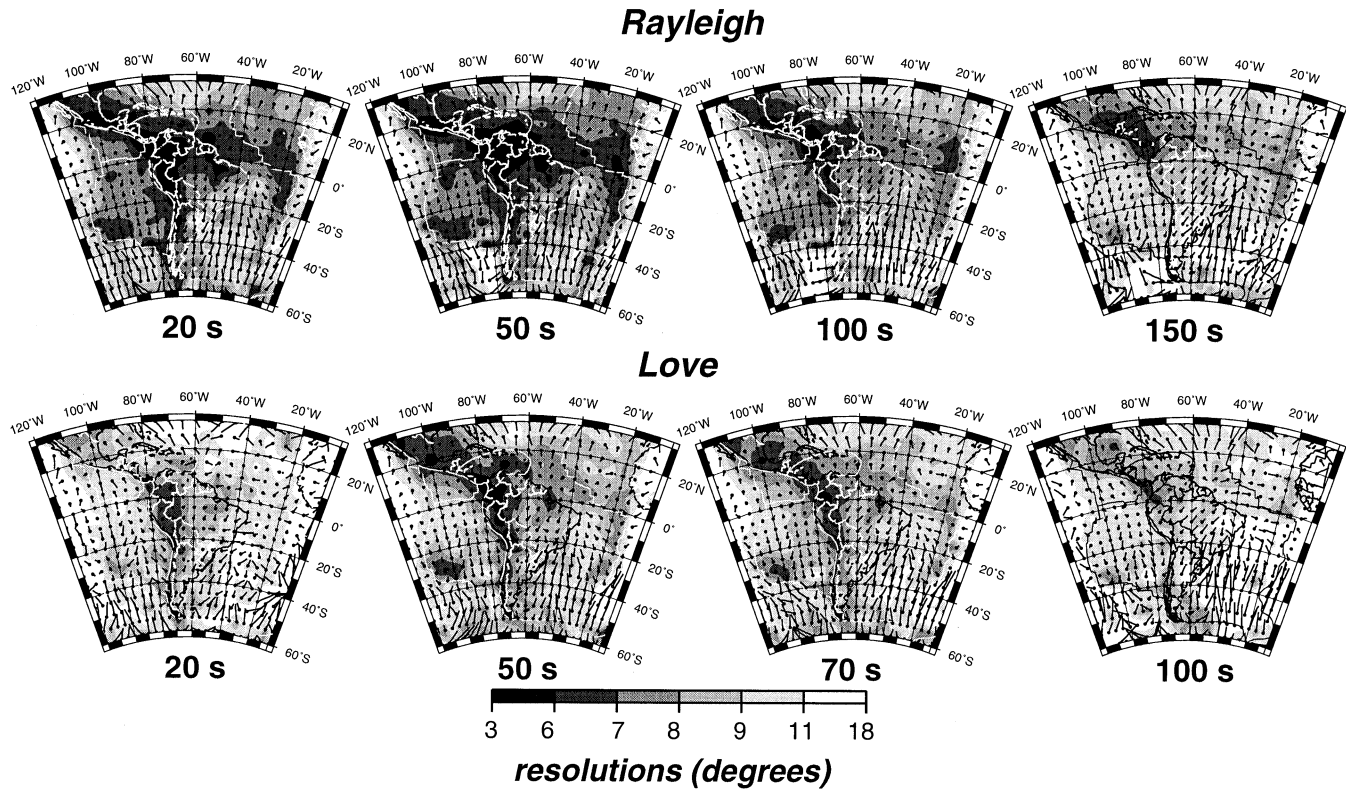
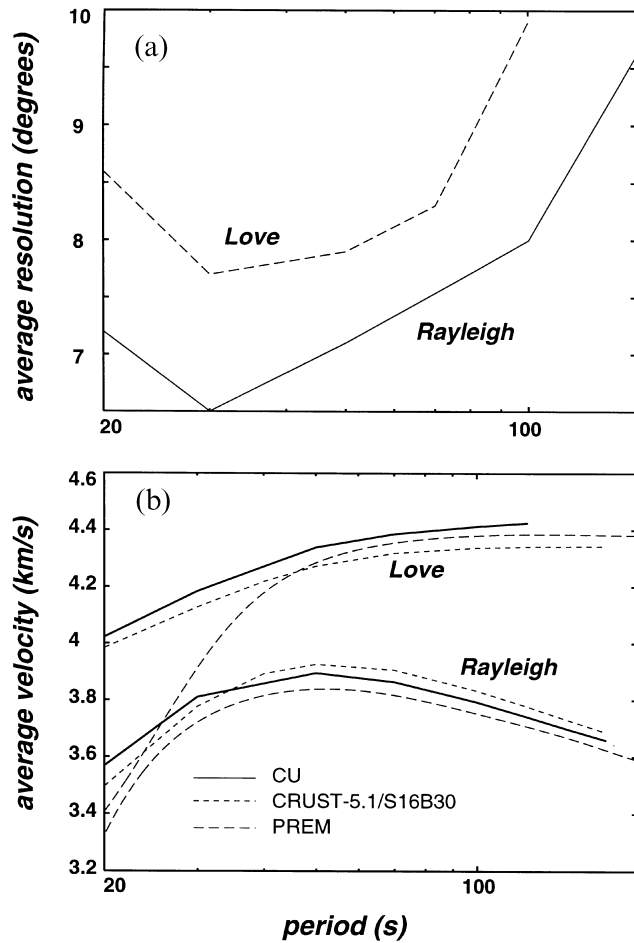


Figure 5. Estimated resolution and bias for Rayleigh and Love waves at the indicated periods. Resolution is grey shaded from 3° to 18°. Bias is represented by black lines that begin at the centroid of the input Gaussian, marked by a black dot, and end at the centroid of the fitted Gaussian.



The maps representing the bias caused by the azimuthal anisotropy in Trampert & Woodhouse’s model are shown in Fig. 7. Bias levels of 1–2 per cent are common, but the bias is most severe off the continent, is stronger for Love than for Rayleigh waves, and is more significant at long periods. This is because azimuthal coverage is more homogeneous on the continent, at short and intermediate periods, and for Rayleigh waves. Biases of several per cent should not be of major concern at periods below about 50 s, but at and above 100 s they may correspond to a significant fraction of the observed anomalies. However, comparison with the observed maps in Figs 8(a) and (b) does not reveal obvious correlations between the locations of anisotropic bias and the major observed group-velocity features. Therefore, we do not believe that the major features that appear in Figs 8(a) and (b) are affected greatly by errors caused by azimuthal anisotropy. Nevertheless, the magnitude of the bias may be appreciable, and simultaneous estimation of isotropic and azimuthally anisotropic velocities is advisable in the future.

4 GROUP-VELOCITY MAPS

Using the tomographic method described in Section 2, we construct group-velocity maps for Rayleigh waves at the

Figure 6. (a) Estimated ‘average’ resolution versus period for Rayleigh (solid) and Love (dashed) waves where the average is taken across the South American continent. (b) Average estimated group-velocity curve across the entire region of study (30°N–60°S, –120°W–0°W; bold solid line) compared with the prediction from PREM (long-dashed line) and from CRUST5.1/S16B30 also averaged across the entire region of study (short-dashed line).

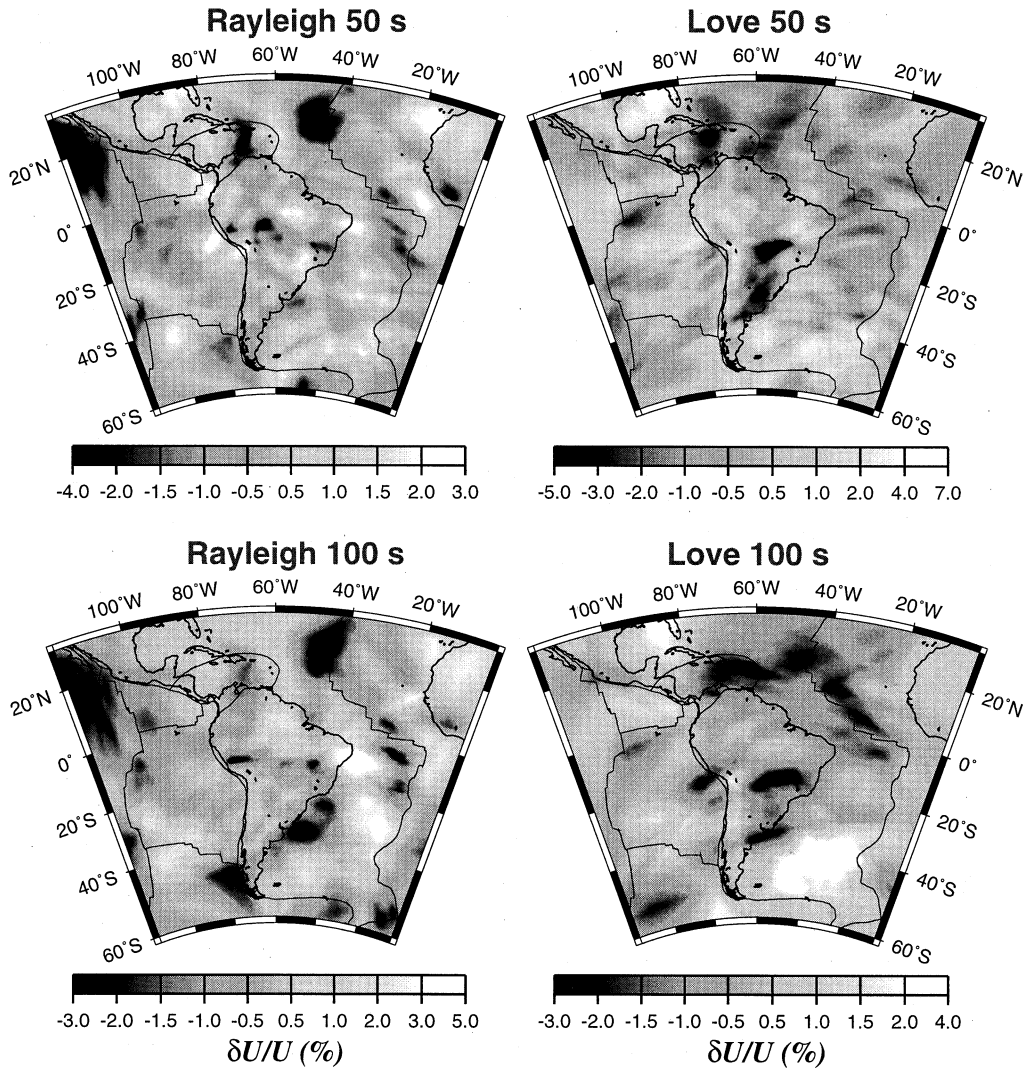


Figure 7. Azimuthal anisotropy bias estimated from the degree 12 anisotropic model of Trampert & Woodhouse (1996). Estimated bias from azimuthal anisotropy expressed as percentage error relative to the average group velocity across the region of study for each period and wave type.

following periods: 20, 25, 30, 35, 40, 50, 60, 70, 80, 90, 100, 125, 150 s. The same periods are inverted for Love waves, except Love-wave group-velocity maps extend only up to 100 s period. Group-velocity curves that represent the average of the group-velocity maps across the studied region (latitude bounds: 60°S–30°N; longitude bounds: 120°W–0°W) for Rayleigh and Love waves are plotted in Fig. 6(b). This figure also presents the group-velocity curves predicted from PREM (Dziewonski & Anderson 1981) and the average of a hybrid aspherical model of the crust (CRUST5.1, Mooney *et al.* 1998) and mantle (S16B30, Masters *et al.* 1996) across the studied region. Since the study region is predominantly oceanic, these averages are more typical of oceanic than of continental crust and upper mantle. This is most clearly indicated by the high-velocity short-period Love wave. The laterally inhomogeneous model (CRUST5.1/S16B30) predicts average group velocities much better than PREM, with a single exception. The group velocities predicted by CRUST5.1/S16B30 are too low for long-period Love waves. This principally results from the fact that CRUST5.1/S16B30 is an isotropic model and the observed

dispersion curves show clear signs of polarization anisotropy (transverse isotropy): Love waves too fast and Rayleigh waves too slow to be fitted by an isotropic model at long periods. The model CRUST5.1/S16B30 provides a better fit to long-period Rayleigh waves than Love waves. It would be difficult for any isotropic model to fit both types of waves well.

Figs 8(a) and (b) present a sample of the estimated group-velocity maps. These maps represent lateral group-velocity variations relative to the regional average of Fig. 6(b). The maps are smoothed *a posteriori* by applying a 2-D Gaussian smoothing filter whose width at the e^{-1} point is 1.5°. A discussion of these maps is the subject of Section 5.

Fig. 9 shows the fit to the measured dispersion curves delivered by the estimated group-velocity maps expressed as two different measures of misfit. The first is variance reduction relative to PREM:

$$\text{Variance reduction} = 1 - \frac{\sum_i (U_i^{\text{obs}} - U_i^{\text{pred}})^2}{\sum_i (U_i^{\text{obs}} - U_0)^2}, \quad (4)$$

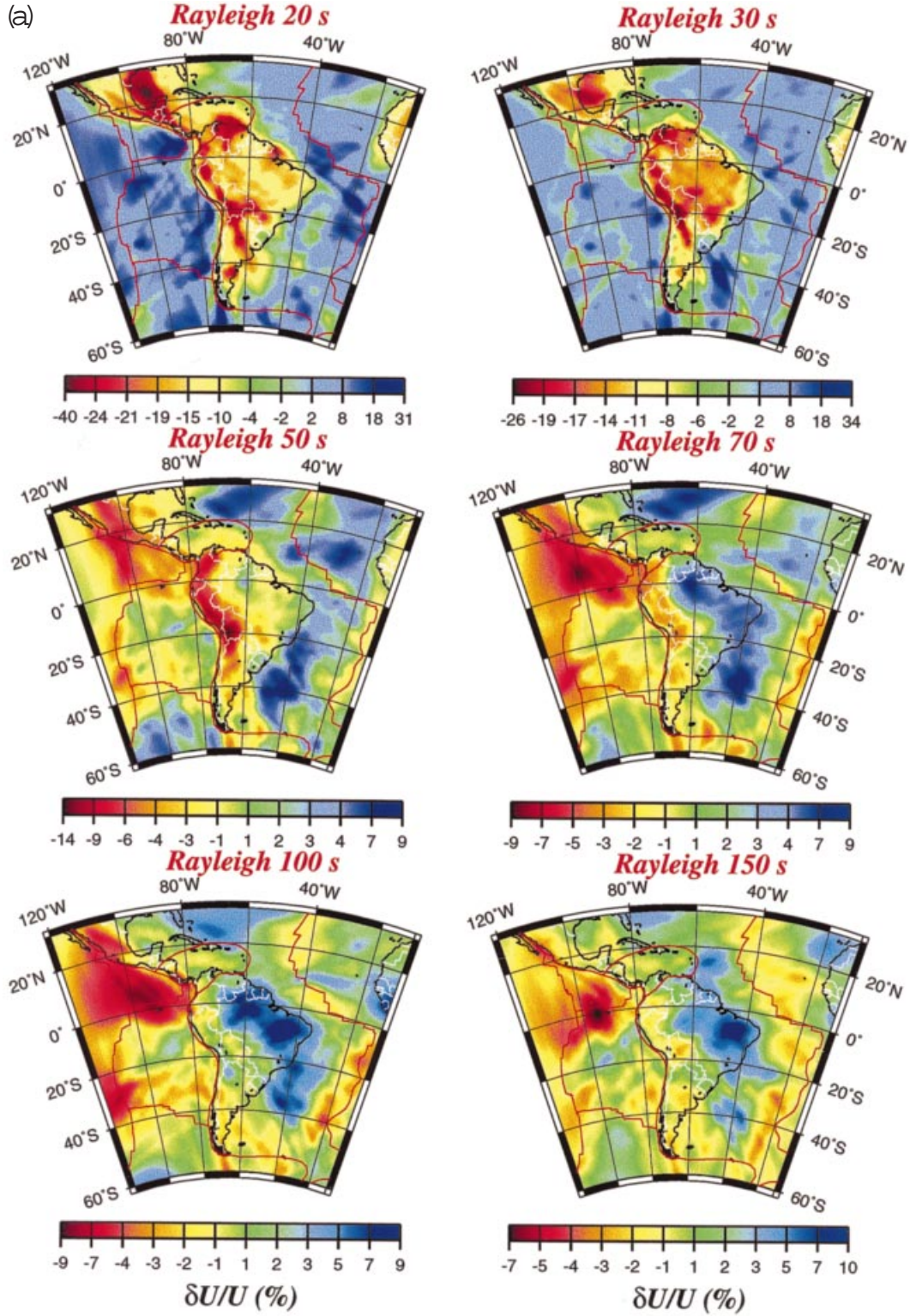


Figure 8. (a) Estimated Rayleigh-wave group-velocity maps at the indicated periods presented in percentage deviation from the averages across the displayed maps (Fig. 6b). (b) Same as (a) but for Love waves at the indicated periods.

where i is the path index, U_i^{pred} is the predicted group velocity for path i through the estimated group-velocity map, U_i^{obs} is the measured group velocity for path i , and U_0 is the reference group velocity from PREM. The second measure of misfit is the rms group-velocity residual:

$$\text{rms velocity misfit} = \left(\frac{1}{N} \sum_i (U_i^{\text{obs}} - U_i^{\text{pred}})^2 \right)^{1/2}, \quad (5)$$

where N is the number of measurements. For each measure

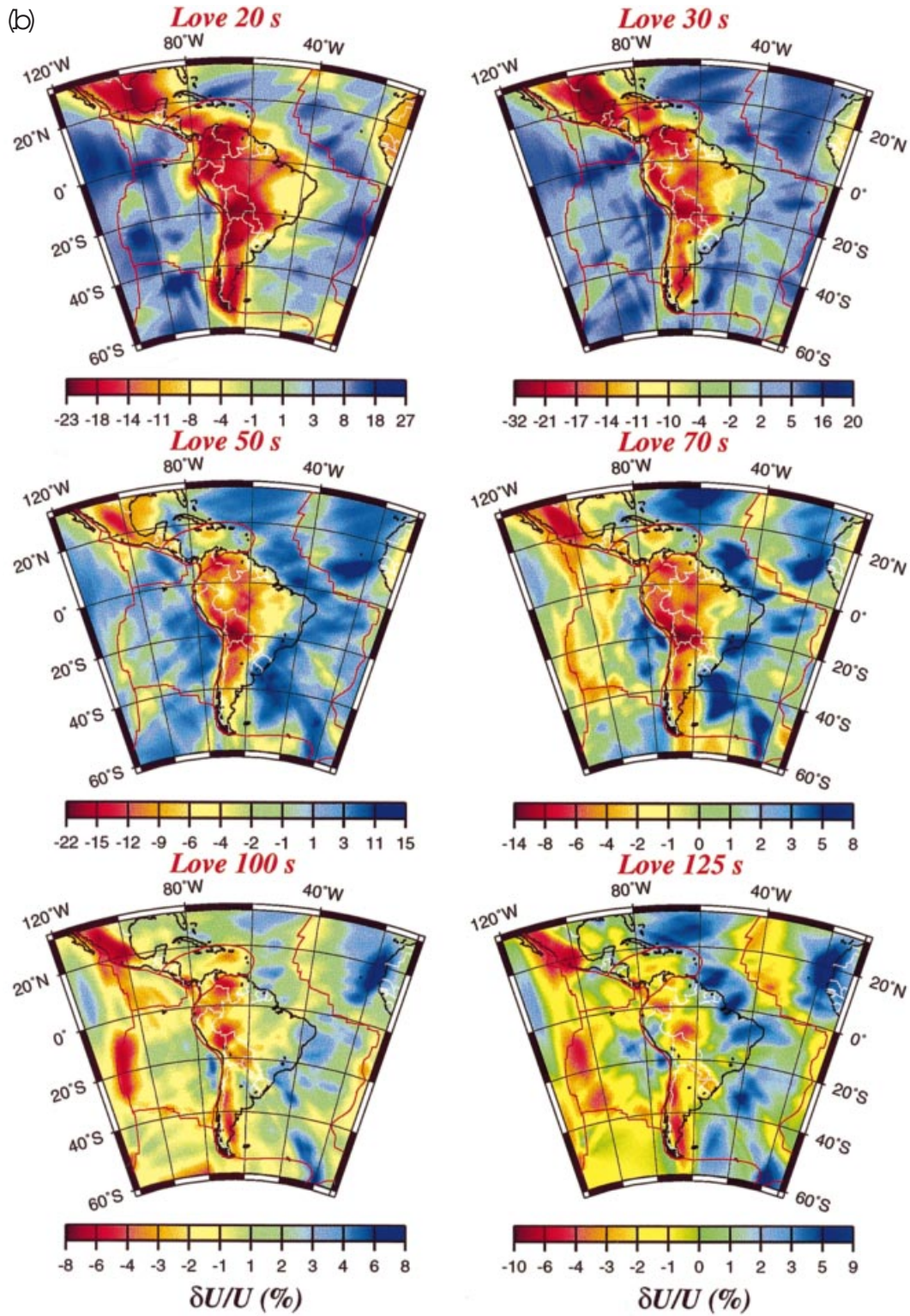


Figure 8. (Continued.)

of misfit, comparison is made between the estimated group-velocity maps and those predicted by the hybrid model CRUST5.1/S16B30.

Variance reductions relative to PREM are more than 90 per cent at short periods and more than 80 per cent at all periods below about 100 s for both Rayleigh and Love waves. Variance

reductions are typically reduced at long periods because lateral variations in the group-velocity maps have smaller amplitudes at longer periods and there is less signal to fit and therefore there is less reduction in variance. Consistent with this is the fact that at the short-period end of the spectrum, absolute misfit is the greatest even though variance reduction continues

to be high. The degradation in misfit below about 40 s period is probably due to off-great-circle propagation and scattering caused by sedimentary basins and other small-scale features. The onset of this degradation in variance reduction is at longer periods for Love waves since they sample more shallowly than Rayleigh waves at every period. For example, the 30 s Love wave is more strongly sensitive to sedimentary features than the 30 s Rayleigh wave. Above 50 s period the absolute misfit is quite flat for both Rayleigh and Love waves, ranging between about 0.04 and 0.06 km s⁻¹.

Measurement uncertainties displayed in Fig. 2(c) are also flat above 50 s period and average between 0.025 and 0.030 km s⁻¹. Thus misfits on average are at about the 1.5–2.0 σ level, where σ is the average measurement uncertainty. The uncertainties reported in Fig. 2(c) are estimates of the repeatability of the measurements, typically for events in the same region. This uncertainty in velocity results principally from difficulties in measuring the time of the arriving wave packet accurately. The remaining misfit between the measurements and the estimated group-velocity maps over and above that caused by measurement errors is likely to result from theoretical errors that include event mislocations at all periods, off-great-circle propagation at the short-period end of the spectrum and azimuthal anisotropy at longer periods.

5 DISCUSSION

Because we believe that the corrupting effects of theoretical errors are at levels below the most striking features on the observed group-velocity maps, it is worthwhile identifying and discussing some of the features that appear to have clear structural causes. The reasons for doing this are to test the geophysical reasonableness of the estimated maps and to illuminate the causative structures of the observed anomalies within the Earth. The interpretation of group-velocity maps is based on the nature of group-velocity sensitivity kernels, some of which are shown in RL98. Group velocity sensitivity kernels are more complicated than phase-velocity sensitivity kernels (e.g. they change sign once with depth) and are compressed nearer to the surface at each period. Group-velocity anomalies, nevertheless, tend to correlate positively with shear-velocity anomalies or boundary topography in the neighbourhood of the positive maximum of the sensitivity kernel. The reason is that the negative excursion in the kernel has lower amplitude, is more limited in depth extent and is typically deeper than the largest positive amplitudes in the kernel. Thus its effect on group velocity is usually relatively unimportant. Because group-velocity sensitivity kernels are complicated functions of radius, any interpretation here should be considered preliminary in nature. It is also important to keep in mind path coverage and resolution (Figs 3 and 5) as well as the effects of theoretical errors, especially azimuthal anisotropy, as discussed in Section 3.2 (Fig. 7).

Group velocity sensitivity may be summarized by several rules of thumb. At a given period, Love waves sample more shallowly than Rayleigh waves and sensitivities for both types of waves compress towards the surface as the period decreases. Both waves are dominantly sensitive to shear velocities. Consequently, everything else being equal, the best probe of sedimentary basins should be the shortest-period Love wave, which here is 20 s. Rayleigh waves between 30 and 75 s are strongly sensitive to lower-crustal velocities and thicknesses,

particularly crustal thickness. The 50 s Rayleigh-wave map, to a fair approximation, can be seen as inversely related to Moho depth. That is, for a 50 s Rayleigh wave, low velocities result largely from thickened crust. Love-wave sensitivity to crustal thickness maximizes between 80 and 100 s period. At longer periods, the sensitivity of waves to crustal velocities and thicknesses diminishes. Uppermost-mantle (80–150 km) shear velocities dominantly affect the 100 s Rayleigh-wave map. The 150 s Rayleigh waves provide sensitivities to shear velocities down to about 200 km depth.

Place names and the outlines of geological and tectonic structures are presented in Fig. 1(b). Fig. 10 presents Rayleigh-wave group-velocity maps predicted by the model CRUST5.1/S16B30 at a variety of periods. The model CRUST5.1 is defined on a 5° grid, and the blocky nature of the predicted group-velocity maps results from the grid defining the model.

5.1 Crustal structures

5.1.1 Sedimentary basins

Everything else being equal, the best indicator of sedimentary basins should be the 20 s Love wave. However, off-pure-path propagation corrupts Love waves more than Rayleigh waves and the Rayleigh-wave resolution is better at 20 s period. Thus, the best indicator of the location and nature of sedimentary basins across South America is the 20 s Rayleigh wave in Fig. 8(a). This map displays four strong low-velocity anomalies in the South American continent in the following locations: (1) western Venezuela and eastern Colombia; (2) northeastern Peru and eastern Ecuador; (3) central and western Bolivia; and (4) eastern Paraguay and far southern Brazil. The first of these anomalies is coincident with the Llanos and Maturin basins, the second with the Marañon-Ucayali-Madre de Dios sedimentary complex, the third with the Altiplano and the Chaco-Tarija Basin, and the fourth with the Chaco-Paraná and southern Paraná basins. Off the continent, a very strong low-velocity anomaly appears in the western Gulf of Mexico associated with the large accumulation of sediments in that region. Low-velocity anomalies appear in the western Caribbean and far eastern Brazil on the 20 s Love-wave map in Fig. 8(b) and appear to be associated with the western Caribbean and Maranhão Basins.

The northern Paraná Basin and the 2500-km-long east–west Amazon Basin are not distinguishable in the tomographic maps. The signature of the Paraná sediments is probably obscured by interpenetrating flood basalts, as in the Tunguska Basin in central Siberia (RL98). It is less clear why the Amazonian sediments do not appear. The two most likely possibilities are that the accumulated sediments are older and faster than younger sediments in the other basins or that the resolution is poor for this elongate east–west feature. Fig. 11(a) presents the results of a synthetic experiment aimed at determining which sedimentary basins should be resolvable. In this simulation we use the 3 km sedimentary contours from the model 3SMAC (Nataf & Ricard 1996) and assign the sediments a uniform 10 per cent group-velocity anomaly, as seen in Fig. 11(a). Using the ray paths, data weighting and damping from the 20 s Rayleigh waves, the estimated structure is shown in Fig. 11(b). The foreland basins in the west as well as the Chaco-Tarija and southern Paraná basins should be the best-resolved basins. Our ability to resolve the Amazon and

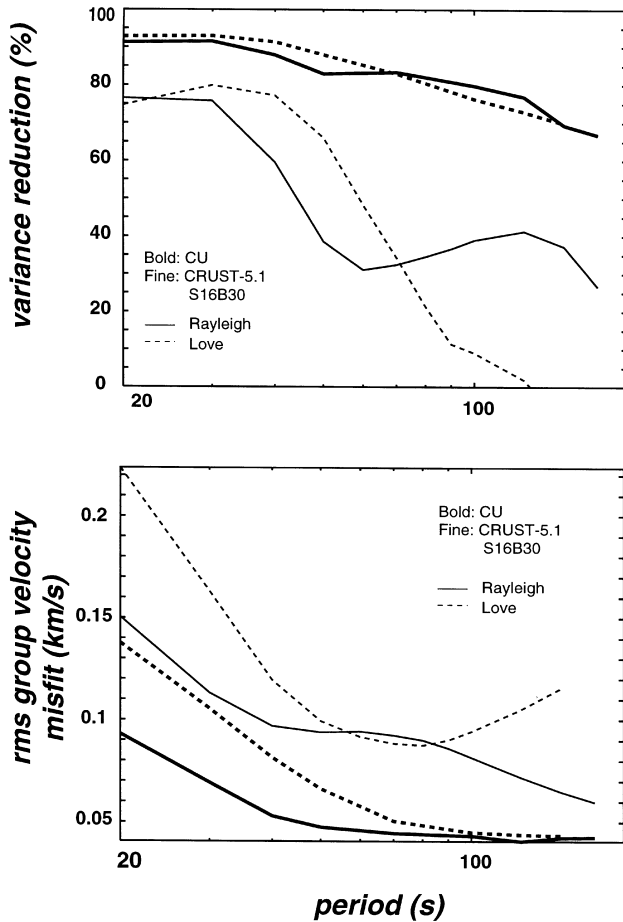


Figure 9. Two measures of misfit to our group-velocity measurements for Rayleigh (solid lines) and Love (dashed lines) waves for two different sets of group-velocity maps. Thick lines are for our group-velocity maps and thin lines are for the group-velocity maps predicted by the model composed of the crustal model CRUST5.1 and the mantle model S16B30. (Top) Misfit is represented as variance reduction relative to the group velocity from PREM. (Bottom) Misfit is the rms group-velocity misfit (eq.).

Maranhão basins is not as good, however. Thus, these basins may not appear on our short-period maps simply because we cannot resolve them. In passing, we point out that off-shore sedimentary basins typically do not appear in group-velocity maps at 20 s period due to the fact that the sensitivity kernels penetrate the mantle. Off-shore sediments are only observable at periods shorter than 20 s unless sedimentary accumulations are exceptionally thick.

Inspection of Fig. 10 reveals that the 20 s Rayleigh-wave map predicted by the model CRUST5.1/S16B30 presents only minimal anomalies in the South American continent. The strongest anomalies are in the Gulf of Mexico and off the northeastern coast of Brazil, due to thick sediments in these regions in CRUST5.1. The low-velocity anomalies of Fig. 8(a) do not appear on the 20 s Rayleigh map from CRUST5.1/S16B30 since most of the basins across South America are too small in size to appear on a gridded $5^\circ \times 5^\circ$ model.

5.1.2 Crustal thickness variations across the continent

The Moho depth is well revealed by the 50 s Rayleigh- and Love-wave maps in Fig. 8. The Rayleigh-wave map is probably

the more reliable of the two due to better path coverage, and generally higher signal-to-noise levels in the data. The 50 s Rayleigh-wave map is dominated by an elongate low-velocity anomaly that runs along nearly the entire western edge of South America following the Andes. Very low velocities extend north from the Altiplano from Bolivia into southern and central Peru and also appear in western Colombia. The magnitude of these low-velocity features is dominantly related to crustal thickness. The strongest low-velocity anomaly and most prominent localized feature of the 50 s Rayleigh- and Love-wave maps is coincident with the Altiplano where the crust is thickest.

In the central Andes of Peru and the northern Andes of Colombia, the 50 s Rayleigh- and Love-wave maps also display pronounced low-velocity anomalies. In the Central Andes, the low-velocity anomaly at 50 s is shifted to the west of the anomaly on the 20 s map, which is consistent with the interpretation that the 50 s anomaly results dominantly from the mountain roots and the 20 s anomaly results from sediments accumulated in folds to the east of the Andes. A similar shrinking and westward shifting of the major low-velocity anomaly with period occurs for the Altiplano region, where the broad, short-period anomaly induced by the Chaco-Tarija Basin shifts west as period increases to eventually give way to a narrow and more pronounced low-velocity anomaly, as longer-period surface waves sense the thickened crust. In the northern Andes, the 50 s low-velocity anomaly is in the area where the Andes range trifurcates ($\sim 7^\circ\text{N}$) to form the west, central and eastern Cordilleras and consequently becoming almost as wide as the Altiplano. In addition to the low-velocity anomalies associated with the Andes and the Altiplano, more subtle low-velocity anomalies on the 50 s Rayleigh-wave map are also associated with the Paraná Basin and the Brazilian Highlands.

Figs 11(c) and 11(d) show an analysis of the ability of the 50 s Rayleigh wave to resolve the group-velocity signal caused by Moho topography underlying the Andes. The amplitude of the input anomaly is constant and, therefore, variation of the amplitude of the retrieved anomaly away from the 10 per cent input amplitude results from poor resolution. In particular, Fig. 11(d) shows that the amplitude of the estimated anomaly is somewhat lower in the narrower northern Andes. However, the amplitude of the low-velocity anomaly on the 50 s Rayleigh-wave map in the northern Andes is actually quite large. It is, therefore, likely that at least part of the amplitude variation of the Andes anomaly observed in Fig. 8(a) results from variations in crustal thickness along the strike of the Andes.

Fig. 10 shows the group-velocity map for the 50 s Rayleigh wave for CRUST5.1/S16B30. Within the limitations of a gridded 5° model, there appears to be pretty good agreement with the observed 50 s map across much of the South American continent. The major exception is that CRUST5.1 misses the low-velocity anomaly under Colombia, which is apparently caused by very thick crust.

5.1.3 Features not observed: massive flood basalts and active volcanic centres

Along the Andes there are three active volcanic centres, none of which appears to produce distinctive velocity anomalies in our short-period group-velocity maps. However, the volcanic centres effectively block the propagation of shorter-period (2–10 s) L_g waves (Rial & Ritzwoller 1997), which suggests

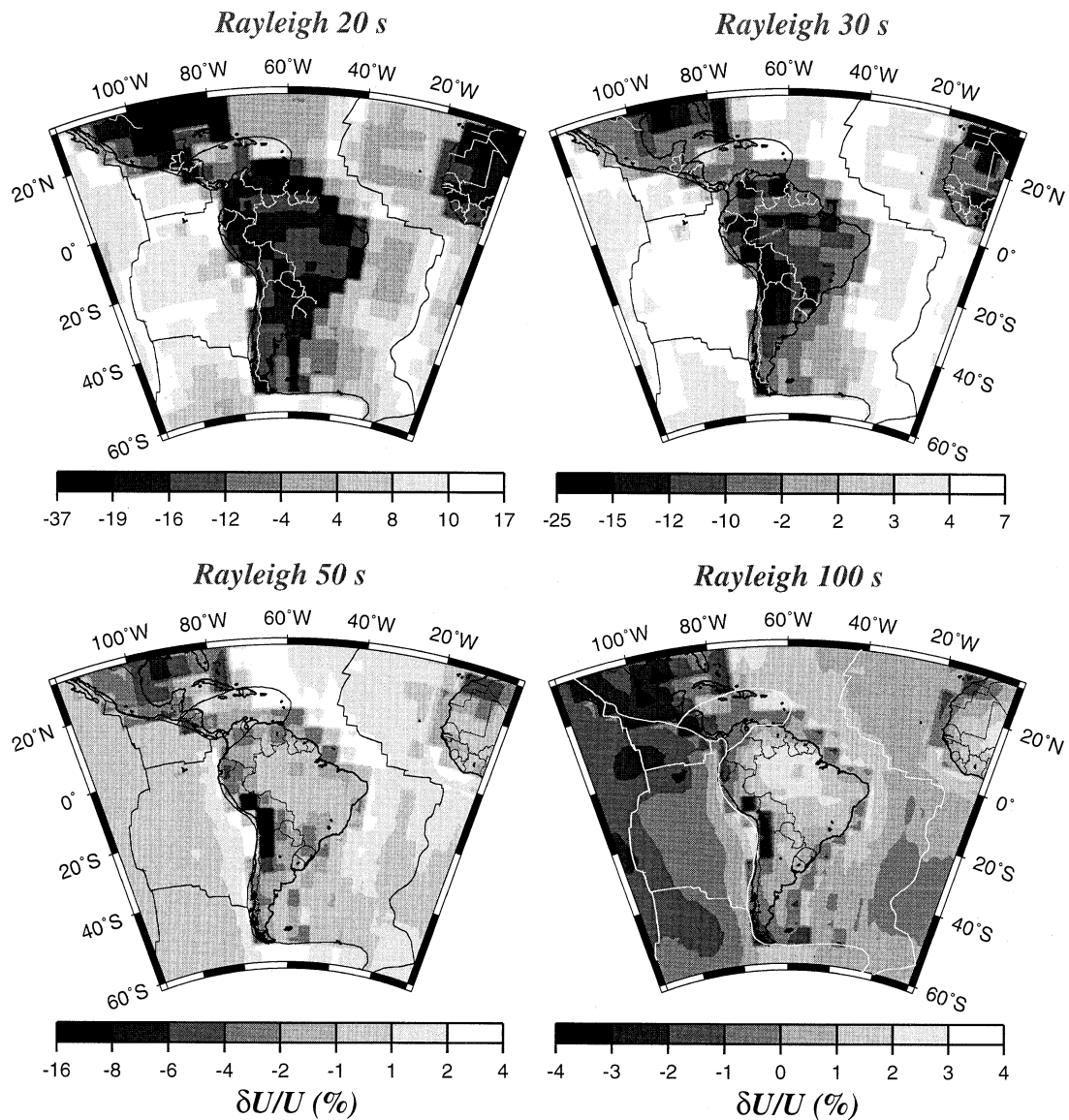
CRUST-5.1/S16B30

Figure 10. Rayleigh-wave group-velocity maps predicted by the model CRUST5.1/S16B30 at the indicated periods presented in percentage deviation from the averages across the observed maps (Fig. 6b).

that their associated magma bodies must be small compared to the wavelength of 20 s Rayleigh or Love waves. RL98 argued that the 20 s maps across Eurasia demonstrated the high-velocity signatures of massive flood basalts. However, the flood basalts of the Paraná Basin do not show a clear imprint on the short-period maps in Fig. 8. The accumulated sediments in the basin probably obscure the signal from the flood basalts on the short- and intermediate-period maps as they do in the Siberian Tunguska Basin (RL98).

5.2 Lithosphere and upper mantle

5.2.1 Cratons and shields

The Proterozoic areas of South America comprise the Amazonian Craton, the Rio de la Plata Craton and the Patagonian Massif. The Amazonian Craton itself is divided

into the Guyana and Guaporé shields and the Sao Francisco Craton. In southeastern Venezuela and north-central Brazil, the Guyana and Guaporé shields are separated by the east–west Amazon Basin. The most prominent high-velocity anomalies in our long-period group-velocity maps (e.g. Rayleigh 100 s) are caused by the presence of the Amazonian Craton. The Rayleigh-wave group-velocity maps display what appears as a somewhat differentiated intracratonic structure on the 80–150 s maps, where at least two separate high-group-velocity nuclei may be distinguished. These nuclei appear to correspond to the Guyana shield, the Guaporé shield, and the Sao Francisco Craton. Resolution analyses such as those in Figs 11(e) and (f) indicate that long-period Rayleigh waves should be able to differentiate these features partially.

Unlike the northern Proterozoic areas, the Patagonian Massif does not appear on the long-period Rayleigh-wave maps as a high-velocity anomaly. In fact, there is a low-velocity

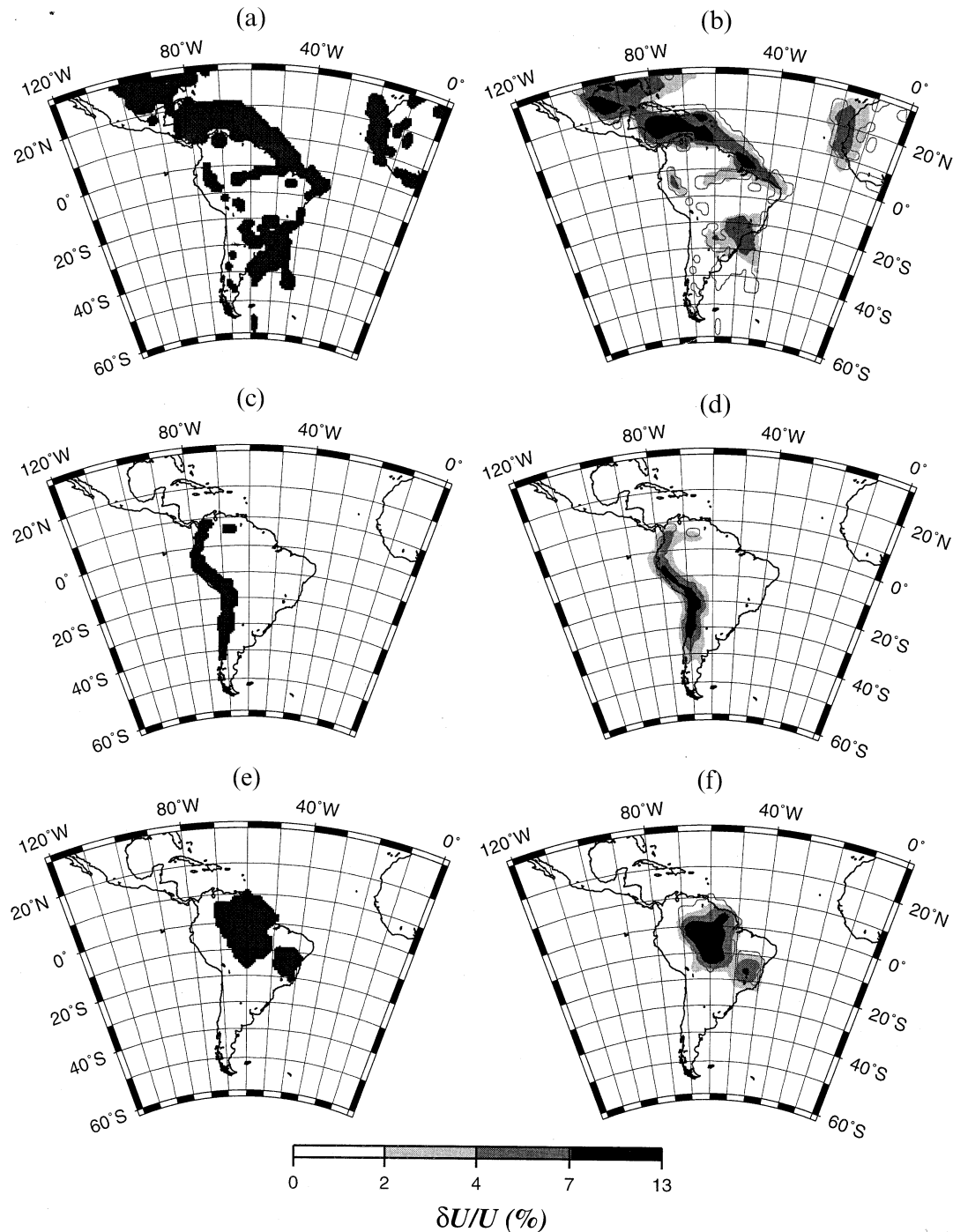


Figure 11. Special resolution analysis for sedimentary basins, Moho topography related to the Andes, and cratonic shields. (a) The input model is the 3 km isopach assigned a velocity perturbation of 10 per cent, taken from 3SMAC (Nataf & Ricard 1996). (b) Estimated map using the paths, weighting and damping for the 20 s Rayleigh wave. (c) The input Moho model is the 44 km contour, taken from 3SMAC (Nataf & Ricard 1996), assigned a velocity perturbation of 10 per cent. (d) Estimated map using the paths, weighting and damping for the 50 s Rayleigh wave. (e) The input cratonic model taken from 3SMAC assigned a velocity perturbation of 10 per cent. (f) Estimated map using the paths, weighting and damping for the 100 s Rayleigh wave. Outlines of the input models are shown as contours in (b), (d) and (f).

anomaly associated with it, particularly for Love waves at periods greater than 60 s. The persistence of this feature and its location under a recognized cratonic region is puzzling.

In Fig. 10, the 100 s Rayleigh-wave group-velocity map from the model CRUST5.1/S16B30 displays the Amazonian Craton as an undifferentiated structure with significantly lower amplitudes than observed in Fig. 8(a).

5.2.2 Oceanic ridges and the Galapagos Hotspot

The low-velocity signature of oceanic ridges only appears unambiguously above about 30 s period for Rayleigh waves and 50 s period for Love waves in Fig. 8. Apparently, the high temperatures associated with ridges are simply over too narrow a region in the crust and uppermost mantle to

affect group velocities appreciably. It is only the larger-scale temperature anomalies at greater depths that contribute to the observed maps. The imprint of the ridges can be seen clearly to the longest periods of this study, although ridge signatures lose some of their continuity and appear to begin to break up somewhat on the 150 s Rayleigh-wave map.

The most spectacular low-velocity feature on any of the maps is the anomaly coincident with the Galapagos Ridge. This anomaly is most pronounced on the long-period Rayleigh-wave maps and is probably caused by an upper-mantle thermal anomaly associated with the Galapagos Hotspot. The 150 s Rayleigh-wave map shows that the thermal anomaly associated with this feature probably extends deeper than the high temperatures associated with other ridges. The deep structure of the Galapagos thermal anomaly is probably not extremely narrow above about 200 km depth, where the long-period Rayleigh waves are sensitive. Otherwise, it would be unable to affect the 150 s Rayleigh wave as strongly as it does.

The mantle model S16B30 possesses the Galapagos anomaly but the amplitude is significantly lower than observed here. Presumably this is because of lower resolution in the global models.

5.2.3 Features not observed: back-arc anomaly, continental plume and subducting plate

Neither subducting lithosphere beneath or adjacent to the Andes (e.g. Engdahl *et al.* 1995, 1997) nor the hypothesized fossil plume beneath southeastern Brazil (VanDecar *et al.* 1995) are observed in the long-period maps in Fig. 8(a). This may be a sensitivity issue. The 100–150 s Rayleigh waves may sample too shallowly (<200 km) to sense these deep features or they may be too small to be resolved. However, it may be the case that these features will manifest themselves upon formal inversion.

Another feature that is not observed is a low-velocity anomaly in the back arc running along the length of the Andes. We might expect this feature because a back-arc low-velocity anomaly is prominent along the entire eastern edge of Asia. The source of the Asian anomaly is contentious. There are at least two competing hypotheses: enrichment in volatiles in the upper mantle by partial melting of the subducting slab and/or the response of the mantle to lithospheric extension. The absence of a South American anomaly means that the mantle near the South American subduction zones differs from the mantle near the east Asian subduction zones. Thus, the source of the Asian anomaly is caused by mantle processes that are different to those in the South American region. This fact may aid future modelling efforts to determine the cause of the Asian anomaly.

5.3 Misfit compared with CRUST5.1/S16B30

Fig. 9 summarizes the fit to the group-velocity measurements delivered by the model CRUST5.1/S16B30 and our group-velocity maps. In Sections 5.1 and 5.2 we discuss the ways in which the group-velocity maps predicted by CRUST5.1/S16B30 differ from the observed maps. All of these differences affect the fit to the group-velocity measurements, but there are probably three discrepancies that have the most significant

affect on misfit. First, intermediate-period Rayleigh waves (40–80 s) are very sensitive to crustal thickness. CRUST5.1/S16B30 predicts group velocities that on average are too high at these periods, indicating that on average the crust is too thin in CRUST5.1 across South America. Because this is true over nearly the entire continent, the cumulative impact on the misfit is appreciable. Second, the Galapagos anomaly is not well resolved in the mantle model S16B30. Therefore, the predicted intermediate- and long-period maps (50–150 s) are also too fast over this large feature. Third, S16B30 is an isotropic model and cannot fit long-period and Rayleigh and Love waves simultaneously. This is the reason for the increase in rms misfit for the long-period Love waves.

6 CONCLUSIONS

We report the results of a systematic study of broad-band Rayleigh- and Love-wave dispersion across South America. There are three main reasons why we believe that this study represents a significant improvement in the understanding of South American surface-wave dispersion. The first concerns the data used. This study is broader band, displays denser and more uniform data coverage, and demonstrates higher resolution than previous studies that have been performed on this scale. Resolutions at most periods average between 6° and 8° across the continent with significantly better resolution in the north and west. Second, the group-velocity maps reveal the signatures of known geological and tectonic features previously not revealed in surface-wave studies of South America. This both lends credibility to the maps and spurs interest in their use to infer future shear-velocity models. Observations at short and intermediate periods (~20–80 s) provide new constraints on shear-velocity models of the crust and on crustal thickness, and the long-period observations (≥100 s) yield higher-resolution constraints on shear-velocity models of the deep lithosphere and upper mantle down to depths of 150–200 km. Finally, the group-velocity maps provide a significant improvement in fit to the observed dispersion curves. This is particularly impressive when compared to misfits from existing South American mantle and crustal models.

Concerning the crust, observed group-velocity anomalies provide new data to constrain future models of sedimentary velocities and thicknesses, crustal velocities and Moho depths. The dispersion signatures of a number of sedimentary basins across the continent, the Caribbean and the western Gulf of Mexico are displayed clearly on the short-period (20–30 s) group-velocity maps (e.g. the Maturin-Llanos, Marañon-Ucayali-Madre de Dios, Chaco-Tarija and Paraná basins in South America). A high-velocity anomaly is not associated with the Paraná flood basalts at short periods, unlike the Deccan Traps and Ethiopian flood basalts of Eurasia (RL98). The sediments in the basin appear to obscure the high-velocity anomaly as they do for the Siberian Tunguska Basin (RL98). One of the most striking features on all of the group-velocity maps is the low-velocity anomalies that appear on both the Rayleigh- (30–90 s) and the Love- (40–125 s) wave maps associated with thickened crust beneath the Andes, the Altiplano and, more subtly, the Brazilian Highlands. Such low-velocity anomalies beneath the Altiplano, in particular, are also observed on recent global phase-velocity maps (e.g. Trampert & Woodhouse 1995; Ekström *et al.* 1997), but the present study provides better resolution and more reliable

amplitude estimates than previous studies. The breadth of the frequency band over which the dispersion maps are produced promises resolution of these crustal structures from one another and from upper-mantle structures during structural inversion for shear-velocity models in the future.

Concerning the uppermost mantle, observed group-velocity anomalies provide new data to constrain the thickness of the lithosphere, the depth extent of mid-ocean ridges and the shear structure of subcontinental roots and the Galapagos Hotspot. The three components of the Amazonian Craton (Guyana shield, Guaporé shield, Sao Francisco Craton) are clearly imaged on the long-period maps, although the smaller southern cratons (Patagonian Massif, Rio de la Plata Craton) are not. The long-period velocity anomaly associated with the Galapagos Ridge is probably the most striking feature on any of the maps. Finally, the absence of low velocities in the Andean back arc at long periods, compared with the east Asian back arc (RL98), provides information about the cause of the Asian anomaly. It results from different physical processes from those in the South American region.

The group-velocity maps we present here provide a substantial improvement in fit to the observed data relative to recent models. They produce a variance reduction relative to PREM of more than 90 per cent at short periods and more than 80 per cent for Rayleigh and Love waves below about 100 s period, which reduces to about 70 per cent at longer periods. rms misfit for the model CRUST-5.1/S16B30 is about 1.5–2 times larger than for the observed maps.

Although we have argued that this study represents a significant step towards understanding South American surface-wave dispersion, there remain significant steps to be taken before the project is completed. The effects of off-great-circle propagation (primarily at short periods) and azimuthal anisotropy (primarily at intermediate and long periods) need to be understood more clearly and probably incorporated in the inversion. Although the bias caused by azimuthal anisotropy may be substantial, it is probably below the levels we discuss here. Second, the future use of data from temporary seismic installations (e.g. BANJO, SEDA, BLSP) would improve resolution on the continent, especially in the east. Finally, the estimated dispersion maps (group and phase) provide important new information to be utilized in future inversions for the shear-velocity structure of the South American crust and uppermost mantle.

All data and maps presented here are available at the following web site: phys-geophys.colorado.edu/geophysics/south_america.dir/south_america.html.

ACKNOWLEDGMENTS

We would like to thank David James, Guust Nolet and Steven Ward for constructive critical reviews that helped to improve this paper, J. Trampert and J.-P. Montagner for providing azimuthal anisotropy models, and G. Laske, W. Mooney, S. Johnson and G. Masters for providing the crustal model CRUST5.1 and the mantle model S16B30. We are particularly grateful to J. Trampert for allowing us to use his model prior to publication, which was the basis for the anisotropic bias experiment. L. Ratnikova, D. Tremblay, M. Silitch and R. Kelly performed most of the dispersion measurements. D. Quinlan and D. Harvey provided a great deal of software and data management advice and support. Much of the data-

base software was written with Datascope (Quinlan 1994). We would like to thank T. B. Yanovskaya and P. G. Ditmar for generously supplying their tomography code. Most of the data were acquired from the IRIS-DMC and the Geoscope Data Center (G. Roullet). All maps were generated with the Generic Mapping Tools (GMT) data processing and display software package (Wessel & Smith 1991, 1995). Aspects of this research were supported by AFOSR contract F49620-95-1-0139 and NSF Office of Polar Programs grant NSF-OPP-9615139.

REFERENCES

- Alsina, D., Woodward, R.L. & Snieder, R.K., 1996. Shear velocity structure in North America from large-scale waveform inversion of surface waves, *J. geophys. Res.*, **101**, 15 969–15 986.
- Backus, G.E. & Gilbert, J.F., 1968. The resolving power of gross earth data, *Geophys. J. R. astr. Soc.*, **16**, 169–205.
- Beck, S., Zandt, G., Myers, S.C., Wallace, T.C., Silver, P.G. & Drake, L., 1996. Crustal-thickness variations in the Central Andes, *Geology*, **24**, 407–410.
- Cara, M., 1973. Filtering of dispersed wave trains, *Geophys. J. R. astr. Soc.*, **33**, 65–80.
- Clark, T.J., Silver, P.G., Yeh, Y.-L., James, D.E., Wallace, T.C. & Beck, S.L., 1995. Close in ScS and sScS reverberations from the 9 June 1994 Bolivian earthquake, *Geophys. Res. Lett.*, **16**, 2313–2316.
- Comte, D., Roecker, S.W. & Suarez, G., 1994. Velocity structure in northern Chile: evidence of subducted oceanic crust in the Nazca Plate, *Geophys. J. Int.*, **117**, 625–639.
- Curtis, A., Dost, B., Trampert, J. & Snieder, R., 1998. Eurasian fundamental mode surface wave phase velocities and their relation to tectonic structures, *J. geophys. Res.*, in press.
- de Souza, J.L., 1995. Shear-wave velocity in the south-eastern Brazilian continental shelf, *Geophys. J. Int.*, **122**, 691–702.
- Ditmar, P.G., & Yanovskaya, T.B., 1987. A generalization of the Backus-Gilbert method for estimation of lateral variations of surface wave velocity, *Izv. AN SSSR, Fizika Zemli (Solid Earth)*, **6**, 30–60 (in Russian).
- Dorbath, C., Granet, M., Poupinet, G. & Martinez, C., 1993. A teleseismic study of the Altiplano and the Eastern Cordillera in Northern Bolivia: new constraints on a lithospheric model, *J. geophys. Res.*, **98**, 9825–9844.
- Dziewonski, A.M. & Anderson, D.L., 1981. Preliminary Reference Earth Model, *Phys. Earth planet Inter.*, **25**, 297–356.
- Dziewonski, A.M., Bloch, S. & Landisman, M., 1969. A technique for the analysis of transient seismic signals, *Bull. seism. Soc. Am.*, **59**, 427–444.
- Dziewonski, A.M., Chou, T.-A. & Woodhouse, J.H., 1981. Determination of earthquake source parameters from waveform data for studies of global and regional seismicity, *J. geophys. Res.*, **86**, 2825–2852.
- Ekström, G., Tromp, J. & Larson, E.W.F., 1997. Measurements and global models of surface wave propagation, *J. geophys. Res.*, **102**, 8137–8158.
- Engdahl, E.R., Van der Hilst, R.D. & Berrocal, J., 1995. Imaging of subducted lithosphere beneath South America, *Geophys. Res. Lett.*, **22**, 2317–2320.
- Engdahl, E.R., Van der Hilst, R.D., Kerby, S. & Widiyantoro, S., 1997. A survey of South American slab structures and internal processes using a new combined data base of high-resolution earthquake hypocenters, tomographic images and focal mechanism data, *EOS, Trans. Am. geophys. Un.*, **78** (46), Fall Meet. Suppl., F446.
- Feng, C.C. & Teng, T., 1983. An error analysis of FTAN, *Bull. seism. Soc. Am.*, **73**, 143–156.
- Friederich, W. & Wielandt, E., 1995. Interpretation of seismic surface waves in regional networks: joint estimation of wavefield geometry

- and local phase velocity. Method and numerical results, *Geophys. J. Int.*, **120**, 731–744.
- Grand, S.P., 1994. Mantle shear structure beneath the Americas and surrounding oceans, *J. geophys. Res.*, **99**, 11 591–11 621.
- Griot, D.A., Montagner, J.P. & Tapponier, P., 1998. Surface wave phase velocity tomography and azimuthal anisotropy in Central Asia, *J. geophys. Res.*, in press.
- James, D.E., 1971. Andean crustal and upper mantle structure, *J. geophys. Res.*, **76**, 3246–3271.
- James, D.E., 1994. P and S seismic velocities in the upper-mantle transition zone beneath the western Brazilian shield, *Extended Abstracts of the International Symposium on the Physics and Chemistry of the Upper Mantle*, pp. 124–126, Brazilian Academy of Sciences and University of São Paulo, São Paulo, Brazil.
- James, D.E. & Assumpção, M., 1996. Tectonic implications of S-wave anisotropy beneath SE Brazil, *Geophys. J. Int.*, **126**, 1–10.
- James, D.E. & Snoke, J.A., 1994. Structure and tectonics in the region of flat subduction beneath central Peru: crust and uppermost mantle, *J. geophys. Res.*, **99**, 6899–6912.
- James, D.E., Assumpção, M., Snoke, J.A., Ribotta, C. & Kuehnel, R., 1993. Seismic studies of continental lithosphere beneath SE Brazil, *Ann. Acad. Bras. Cien.*, **65**, suppl. 2, 227–250.
- Knopoff, L. & Schwab, F.A., 1968. Apparent initial phase of a source of Rayleigh waves, *J. geophys. Res.*, **73**, 755–760.
- Landisman, M., Dziewonski, A. & Sato, Y., 1969. Recent improvements in the analysis of surface wave observations, *Geophys. J. R. astr. Soc.*, **17**, 369–403.
- Larson, E.W., Tromp, J. & Ekstrom, G., 1997. Effects of slight anisotropy on surface waves, *J. geophys. Res.*, **102**, 8137–8154.
- Laske, G. & Masters, G., 1996. Constraints on global phase velocity maps from long-period polarization data, *J. geophys. Res.*, **101**, 16 059–16 075.
- Lévêque, J.-J., Rivera, L. & Wittlinger, G.W., 1993. On the use of the checkerboard test to assess the resolution of tomographic inversions, *Geophys. J. Int.*, **115**, 313–318.
- Levshin, A.L., Pisarenko, V.F. & Pogrebinsky, G.A., 1972. On a frequency-time analysis of oscillations, *Ann. Geophys.*, **28**, 211–218.
- Levshin, A.L., Yanovskaya, T.B., Lander, A.V., Bukchin, B.G., Barmin, M.P., Ratnikova, L.I. & Its, E.N., 1989. *Seismic Surface Waves in a Laterally Inhomogeneous Earth*, ed. Keilis-Borok, V.I., Kluwer, Dordrecht.
- Levshin, A.L., Ratnikova, L. & Berger, J., 1992. Peculiarities of surface wave propagation across central Eurasia, *Bull. seism. Soc. Am.*, **82**, 2464–2493.
- Li, X.D. & Romanowicz, B., 1996. Global mantle shear velocity model developed using nonlinear asymptotic coupling theory, *J. geophys. Res.*, **101**, 22 245–22 272.
- Masters, G., Johnson, S., Laske, G. & Bolton, H., 1996. A shear-velocity model of the mantle, *Phil. Trans. R. Soc. Lond.*, **A354**, 1385–1411.
- Montagner, J.P. & Tanimoto, T., 1991. Global upper mantle tomography of seismic velocities and anisotropies, *J. geophys. Res.*, **96**, 20 337–20 351.
- Mooney, W.D., Laske, G. & Masters, G., 1998. CRUST 5.1: a global crustal model at 5 degrees by 5 degrees, *J. geophys. Res.*, **103**, 727–748.
- Myers, S., Beck, S., Zandt, G. & Wallace, T., 1995. Mantle seismic attenuation in the Bolivian Andes; evidence for partial melt in the shallow mantle under the Altiplano, *EOS, Trans. Am. geophys. Un.*, **76** (46), 373.
- Nataf, H.-C. & Ricard, Y., 1996. 3SMAC: an a priori tomographic model of the upper mantle based on geophysical modeling, *Phys. Earth planet Inter.*, **95**, 101–122.
- Quinlan, D.M., 1994. Datascope: a relational database system for scientists, *EOS, Trans. Am. geophys. Un.*, **75**, F431.
- Rial, J.A. & Ritzwoller, M.H., 1997. Propagation Efficiency of Lg waves in South America, *Geophys. J. Int.*, **131**, 401–408.
- Ritzwoller, M.H. & Levshin, A.L., 1998. Eurasian surface wave tomography: group velocities, *J. geophys. Res.*, **103**, 4839–4878.
- Ritzwoller, M.H., Levshin, A.L., Ratnikova, L.I. & Egorkin, A.A., 1998. Intermediate-period group-velocity maps across Central Asia, western China and parts of the Middle East, *Geophys. J. Int.*, **134**, 315–328.
- Russell, D.W., Herrman, R.B. & Hwang, H., 1988. Application of frequency-variable filters to surface wave amplitude analysis, *Bull. seism. Soc. Am.*, **78**, 339–354.
- Snieder, R., 1988. Large-scale waveform inversion of surface waves for lateral heterogeneity, 2. Application to surface waves in Europe and the Mediterranean, *J. geophys. Res.*, **93**, 12 067–12 080.
- Snoke, J.A. & James, D.E., 1997. Lithospheric structure of the Chaco and Paraná basins of South America from surface-wave inversion, *J. geophys. Res.*, **102**, 2939–2951.
- Su, W., Woodward, R.L. & Dziewonski, A.M., 1994. Degree 12 model of shear velocity heterogeneity in the mantle, *J. geophys. Res.*, **99**, 6945–6980.
- Trampert, J. & Woodhouse, J., 1995. Global phase velocity maps of Love and Rayleigh waves between 40 and 150 seconds, *Geophys. J. Int.*, **122**, 675–690.
- Trampert, J. & Woodhouse, J., 1996. Global azimuthal anisotropy, *Eur. Geophys. Soc. Newslett.*, **58**, 57.
- Van der Lee, S. & Nolet, G., 1997a. Seismic image of the subducted trailing fragments of the Farallon plate, *Nature*, **386**, 266–269.
- Van der Lee, S. & Nolet, G., 1997b. Upper mantle S velocity structure of North America, *J. geophys. Res.*, **102**, 22 815–22 838.
- Van der Lee, S., James, D. & Silver, P., 1997. Upper-mantle S-velocity structure of South America from portable and permanent seismic networks, *EOS, Trans. Am. geophys. Un.*, **78** (46), Fall Meet. Suppl., F446.
- VanDecar, J.C., James, D.E. & Assumpção, M., 1995. Seismic evidence for a fossil mantle plume beneath South America and implications for plate driving forces, *Nature*, **378**, 25–31.
- Wessel, P. & Smith, W.H.F., 1991. Free software helps map and display data, *EOS, Trans. Am. geophys. Un.*, **72**, 441.
- Wessel, P., & Smith, W.H.F., 1995. New version of the Generic Mapping Tools released, *EOS, Trans. Am. geophys. Un.*, **76**, 329.
- Wielandt, E., 1993. Propagation and structural interpretation of non-plane waves, *Geophys. J. Int.*, **113**, 45–53.
- Wigger, P.J. et al., 1994. Variation in the crustal structure of the southern Central Andes deduced from seismic refraction investigations, in *Tectonics of the Southern Central Andes*, pp. 23–48, eds Reutter, K.J., Schenber, E. & Wigger, P.J., Springer-Verlag, Berlin.
- Yanovskaya, T.B. & Ditmar, P.G., 1990. Smoothness criteria in surface-wave tomography, *Geophys. J. Int.*, **102**, 63–72.
- Zandt, G., Beck, S.L., Ruppert, S.R., Ammon, C.J., Rock, D., Minaya, E., Wallace, T.C. & Silver, P.G., 1995. Anomalous crust of the Bolivian Altiplano, Central Andes: constraints from broad-band regional seismic waveforms, *Geophys. Res. Lett.*, **23**, 1159–1162.
- Zhang, Y.S. & Tanimoto, T., 1993. High resolution global upper mantle structure and plate tectonics, *J. geophys. Res.*, **98**, 9793–9823.